

Fast Sodium Storage in $\text{TiO}_2@\text{CNT}@\text{C}$ Nanorods for High-Performance Na-Ion Capacitors


Yuan-En Zhu, Leping Yang, Jian Sheng, Yanan Chen, Haichen Gu, Jinping Wei,* and Zhen Zhou*

Na-ion capacitors have attracted extensive interest due to the combination of the merits of high energy density of batteries and high power density as well as long cycle life of capacitors. Here, a novel Na-ion capacitor, utilizing $\text{TiO}_2@\text{CNT}@\text{C}$ nanorods as an intercalation-type anode and biomass-derived carbon with high surface area as an ion adsorption cathode in an organic electrolyte, is reported. The advanced architecture of $\text{TiO}_2@\text{CNT}@\text{C}$ nanorods, prepared by electrospinning method, demonstrates excellent cyclic stability and outstanding rate capability in half cells. The contribution of extrinsic pseudocapacitance affects the rate capability to a large extent, which is identified by kinetics analysis. A key finding is that ion/electron transfer dynamics of $\text{TiO}_2@\text{CNT}@\text{C}$ could be effectively enhanced due to the addition of multiwalled carbon nanotubes. Also, the biomass-derived carbon with high surface area displays high specific capacity and excellent rate capability. Owing to the merits of structures and excellent performances of both anode and cathode materials, the assembled Na-ion capacitors provide an exceptionally high energy density (81.2 W h kg^{-1}) and high power density ($12\,400 \text{ W kg}^{-1}$) within 1.0–4.0 V. Meanwhile, the Na-ion capacitors achieve 85.3% capacity retention after 5000 cycles tested at 1 A g^{-1} .

1. Introduction

As the escalating fossil energy crisis, the contradiction between the growing energy demand and the absence of fossil fuels becomes increasingly prominent. Therefore, developing next-generation large-scale energy storage devices with both high energy and power density is urgent for the application to electric vehicles and smart grids.^[1,2] Supercapacitors with the merits of large power output and long cycle life have been extensively explored and achieved rapid development in recent years.

Y.-E. Zhu, L. P. Yang, J. Sheng, Y. N. Chen, H. C. Gu, Prof. J. P. Wei, Prof. Z. Zhou
Institute of New Energy Material Chemistry
Collaborative Innovation Center of Chemical Science and Engineering (Tianjin)
School of Materials Science and Engineering
National Institute for Advanced Materials
Nankai University
Tianjin 300350, China
E-mail: jpwei@nankai.edu.cn; zhouzhen@nankai.edu.cn

 The ORCID identification number(s) for the author(s) of this article can be found under <https://doi.org/10.1002/aenm.201701222>.

DOI: 10.1002/aenm.201701222

However, low operation voltage due to water splitting severely limits their energy density.^[3–6] Hence, developing organic electrolyte systems could efficiently extend the electrochemical window for high energy density.^[7] Accordingly, lithium-ion batteries (LIBs) with wider electrochemical window in organic electrolytes guarantee higher energy density. However, lithium sources are limited, and the increasing price has confined large-scale utilizations.^[8] Consequently, owing to the electrochemical equivalent characteristics and rich resources of sodium, sodium-ion batteries (SIBs) attract great interest and would become low-cost energy storage devices alternative to LIBs.^[9–11] Unfortunately, lithium/sodium ion batteries exhibit poor power density and relatively inferior service life.

Na^+ ions, with larger radius (r_{Na^+} : 1.02 \AA ; r_{Li^+} : 0.76 \AA), tend to surface pseudocapacitive processes, which is preferable for Na-ion capacitors.^[12] As the bridge that links batteries and capacitors

in organic electrolytes, Na-ion capacitors emerge with different storage mechanisms at both ends.^[13–17] Unlike SIBs, which mainly depend on the migration of Na^+ between the anode and cathode, Na-ion capacitors are composed of battery-type anodes and capacitor-type cathodes. In the charging process, Na^+ migrates to the anode (faradaic reactions), and meanwhile anions in the electrolyte (such as ClO_4^-) migrate and adsorb to the cathode surface (nonfaradaic reactions). In the discharging process, Na^+ and ClO_4^- come back into electrolytes again. Commercial activated carbon (AC) was commonly selected as the cathode material for Na-ion capacitors. Insertion-type battery materials with pseudocapacitance were adopted as the anode of Na-ion capacitors, owing to the moderate reversible capacity, rapid faradic reaction, low volume variation, and stable structure upon sodium ion insertion/extraction.^[18] Recently, Wang group^[19] has reported Na-TNTs (sodium titanate nanotubes) as anode materials for Na-ion capacitors. Thangavel et al.^[20] assembled C-NVP//CDC, with NASICON-type $\text{Na}_3\text{V}_2(\text{PO}_4)_3/\text{C}$ as the anode material and high-surface-area AC as the cathode material, which showed excellent cyclic stability, but lower electrochemical window (0–3 V) severely limits the energy density of the devices. Lim et al.^[13] reported that $\text{Nb}_2\text{O}_5@\text{C}/\text{rGO}/\text{MSP}$ Na-ion capacitors with $\text{Nb}_2\text{O}_5@\text{C}/\text{rGO}$ anodes and commercial AC cathodes exhibited higher energy density at lower current

density in the voltage range of 1–4.3 V. However, the cyclability and rate performance were moderate. Despite great progress has been made these years, low capacity and rapid fading of anode materials are still the major impediment to optimize Na-ion capacitors.^[13,18,21,22] Designing and preparing new suitable insertion-type anode materials to match suitable cathode materials for Na-ion capacitors is extremely urgent.

TiO₂ can serve as an insertion-type anode material with obvious superiority in SIBs.^[23–26] As we know, TiO₂ has a lower average potential for Na storage (0.7 V vs Na/Na⁺), which is more beneficial to improve energy density in Na-ion capacitors. Furthermore, the inherent pseudocapacitive behavior of TiO₂ is a major advantage to promote the electrochemical performances of Na-ion capacitors. Nevertheless, TiO₂ is a semiconductor, which leads to poor electronic conductivity ($\approx 10^{-12}$ S cm⁻²) and sluggish ionic diffusivity. Hence, massive efforts have been made to enhance ion/electron conduction. Heteroatom doping (N, S, or Nb),^[25,27,28] surface coating (graphitized carbon or graphene),^[29,30] morphology control (petal-like, quantum dot, or nanofiber morphology),^[30–33] and so on, have proved effectively in boosting the conductivity of the composites. Huang and co-workers^[29] reported that TiO₂/rGO composites exhibited fast Na⁺ insertion/extraction, which occurred not only on the surface but also in the bulk of the material. Ji and co-workers^[30] synthesized graphene-wrapped petal-like rutile TiO₂ tuned with carbon dots, delivering excellent cyclability and rate capability. Therefore, TiO₂ is an ideal anode material for Na-ion capacitors.

On the other hand, highly porous activated carbon has been widely explored as a nonfaradaic cathode material for Na-ion

capacitors because of their large specific surface area and fast electron/ion transport.^[5] Especially, researchers have paid more attention to biomass-derived activated carbon because of its low cost and eco-friendliness. However, to date, the reports on the cyclability and capacitance at high-power conditions of activated carbon materials are still very scarce. Consequently, a suitable activated carbon material with high surface areas and stable architectures is also highly desired as the cathode material for Na-ion capacitors.

Herein, by means of a facile electrospinning technique, we successfully designed and prepared a novel architecture of TiO₂@CNT@C, which can serve as the high-energy/power anode material for Na-ion capacitors. Benefiting from the introduction of multiwalled carbon nanotubes (MWCNTs), the TiO₂@CNT@C electrode exhibited superior rate capability and cyclic stability in half cells. Furthermore, with this composite as the anode and biomass-derived carbon as the cathode, the newly configured Na-ion capacitors presented an exceptionally high energy and power density as well as long cycling stability.

2. Results and Discussion

TiO₂@CNT@C nanorods were successfully prepared through a facile electrospinning technique, with one-step incorporating MWCNTs into TiO₂ nanorods. TiO₂@C was the control sample without the addition of MWCNTs. The X-ray diffraction (XRD) patterns of TiO₂@CNT@C and TiO₂@C are shown in Figure 1a. The diffraction peaks of both samples are well indexed to anatase TiO₂ with the *I4₁/amd* space group. The

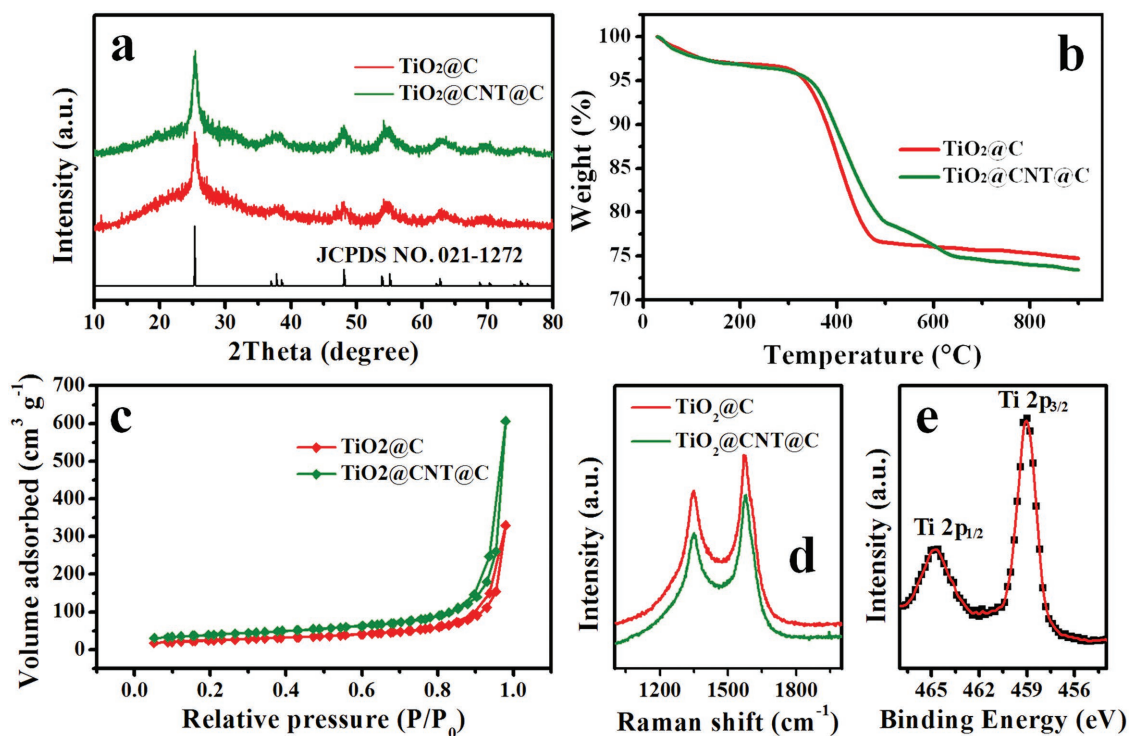


Figure 1. Structural characterizations of TiO₂@CNT@C and TiO₂@C. a) XRD patterns, b) TGA, c) N₂ adsorption–desorption isothermal curves, d) Raman spectra of TiO₂@CNT@C and TiO₂@C, and e) high-resolution XPS of Ti2p in the TiO₂@CNT@C sample.

weak intensity of the TiO_2 peaks in XRD patterns is ascribed to highly distributed TiO_2 nanoparticles embedded in the carbon matrix. Thermogravimetric analysis (TGA) was measured to determine the TiO_2 content in the as-prepared samples, as shown in Figure 1b. $\text{TiO}_2@\text{C}$ and $\text{TiO}_2@\text{CNT}@\text{C}$ have 25 and 27 wt% weight loss, respectively, suggesting 75 wt% TiO_2 in $\text{TiO}_2@\text{C}$ and $\approx 73\%$ TiO_2 in $\text{TiO}_2@\text{CNT}@\text{C}$. Interestingly, compared with $\text{TiO}_2@\text{C}$, $\text{TiO}_2@\text{CNT}@\text{C}$ shows a sloping region between 480 and 600 °C in the TGA curve, which might be related to the oxidation of MWCNTs. It is an obvious proof that MWCNTs exist in the final composite and the content of it in $\text{TiO}_2@\text{CNT}@\text{C}$ is $\approx 1.5\text{--}2$ wt%. N_2 adsorption–desorption measurements were performed and the results are shown in Figure 1c. The Brunauer–Emmett–Teller (BET) surface areas of $\text{TiO}_2@\text{CNT}@\text{C}$ and $\text{TiO}_2@\text{C}$ are 135 and 85 $\text{m}^2 \text{g}^{-1}$, respectively. Figure S1 (Supporting Information) shows the pore distribution of two samples; $\text{TiO}_2@\text{CNT}@\text{C}$ has more abundant meso- and micropores than $\text{TiO}_2@\text{C}$, mainly due to the addition of MWCNTs. Figure 1d presents the Raman spectra of $\text{TiO}_2@\text{CNT}@\text{C}$ and $\text{TiO}_2@\text{C}$. The two prominent peaks at ≈ 1349 and $\approx 1580 \text{ cm}^{-1}$ are attributed to a disorder-induced feature (D band) and the $\text{E}_{2\text{g}}$ mode of graphite (G band),^[34] respectively. The intensity ratio of D versus G band ($I_{\text{D}}/I_{\text{G}}$) is 0.836 and 0.794 for $\text{TiO}_2@\text{C}$ and $\text{TiO}_2@\text{CNT}@\text{C}$, respectively, which represents the structural imperfection of graphitic sp^2 domains of carbon materials. A certain degree of graphitization ($I_{\text{D}}/I_{\text{G}} < 1$) guarantees high-quality electrical conductivity.^[35] The surface element composition and valence of $\text{TiO}_2@\text{CNT}@\text{C}$ were determined by X-ray photoelectron spectroscopy (XPS), as shown in Figure 1e. The two peaks at about 464.6 and 458.9 eV are contributed from $\text{Ti}2\text{p}_{1/2}$ and $\text{Ti}2\text{p}_{3/2}$, respectively,^[36] which confirms that the valence of Ti is +4.

Figure 2a,b shows the schematic diagram of $\text{TiO}_2@\text{CNT}@\text{C}$ and $\text{TiO}_2@\text{C}$. Figure 2c displays the scanning electron microscope (SEM) images of $\text{TiO}_2@\text{CNT}@\text{C}$ nanorods. The diameter of $\text{TiO}_2@\text{CNT}@\text{C}$ nanorods is about 200–300 nm and the length is not unified. The surfaces of $\text{TiO}_2@\text{CNT}@\text{C}$ nanorods are very rough with many microscopic voids, which might bring more active sites for electrode surface reactions. With randomly distributed nanorods, this architecture would be beneficial to link the electrode materials and electrolytes and boost the rapid transfer of Na^+/e^- .^[37] In addition, there is no apparent difference in the surface morphology between $\text{TiO}_2@\text{CNT}@\text{C}$ and $\text{TiO}_2@\text{C}$ (Figure 2c,d), elucidating that the introduction of MWCNTs would not change the morphology of $\text{TiO}_2@\text{C}$. Note that MWCNTs were not detected from the SEM image of

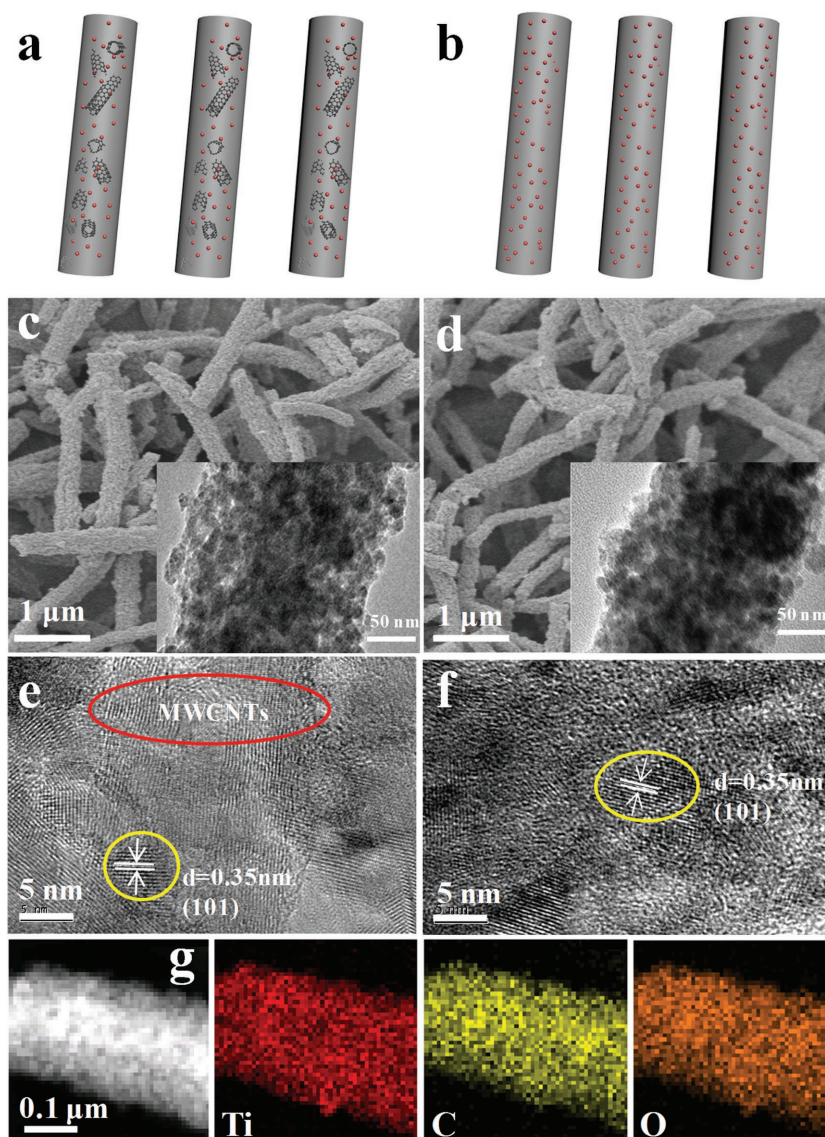


Figure 2. Schematic diagrams of a) $\text{TiO}_2@\text{CNT}@\text{C}$ and b) $\text{TiO}_2@\text{C}$. SEM images of c) $\text{TiO}_2@\text{CNT}@\text{C}$ and d) $\text{TiO}_2@\text{C}$; HRTEM images of e) $\text{TiO}_2@\text{CNT}@\text{C}$ and f) $\text{TiO}_2@\text{C}$; g) TEM elemental mapping images of $\text{TiO}_2@\text{CNT}@\text{C}$. The insets in (c) and (d) are TEM images of $\text{TiO}_2@\text{CNT}@\text{C}$ and $\text{TiO}_2@\text{C}$, respectively.

$\text{TiO}_2@\text{CNT}@\text{C}$, suggesting that MWCNTs might be embedded into the TiO_2 and C matrix. The detailed structures of $\text{TiO}_2@\text{CNT}@\text{C}$ nanorods were further characterized by transmission electron microscope (TEM) (inset in Figure 2c,d). TiO_2 nanoparticles are felicitously embedded in carbon nanorods. The nanoscale structure will be greatly conducive to release more pseudocapacitance of active materials.^[38] The high-resolution TEM (HRTEM) images (Figure 2e,f) reveal the clear lattice fringes with a d -spacing of 0.35 nm, corresponding to the (101) planes of anatase-phase TiO_2 . The HRTEM images show that the average size of TiO_2 nanocrystals is ≈ 6.9 nm in $\text{TiO}_2@\text{CNT}@\text{C}$ (Figure S2, Supporting Information). By using Scherrer equation, we estimated the crystalline size of TiO_2 nanocrystals to be ≈ 14.4 nm on basis of the XRD data (Table S1, Supporting Information), which is larger than that of

the HRTEM observation. The result is coincident with the previous report.^[39] Moreover, MWCNTs are clearly visualized in the HRTEM image (Figure 2e, and Figure S2, Supporting Information), which further confirms that MWCNTs were incorporated into TiO₂ and carbon nanorods. The TEM mapping images of TiO₂@CNT@C nanorods in Figure 2g show that TiO₂ nanoparticles are homogeneously distributed in the specimen. The stable external carbon frame and internal MWCNT network would be beneficial for electrochemical performances.

The electrochemical performances of TiO₂@CNT@C electrodes were tested in sodium half cells with metallic sodium as the counter electrodes. Figure 3a shows cyclic voltammetric (CV) curves for TiO₂@CNT@C at the scan rate of 0.1–8 mV s⁻¹ in the range of 0.01–2.5 V (vs Na/Na⁺), and the initial several CV curves at 0.1 mV s⁻¹ are shown in Figure S3a (Supporting Information). A couple of broad cathode/anode peaks are located at 0.70/0.85 V, corresponding to the reversible reaction of Ti³⁺/Ti⁴⁺ for the sodiation/desodiation processes. Moreover, the CV curves exhibit similar shapes at various scan rates. According to the relationship between the peak current density (*i*) and the scan rate (*v*)^[40]

$$i = av^b \quad (1)$$

In Equation (1), the *b*-value represents the slope of the log(*v*)-log(*i*) plots. Especially, the slope of 0.5 (*b* = 0.5) signifies a diffusion-controlled process, and the slope of 1 (*b* = 1) suggests the capacitive-controlled behavior (also named surface Faradic redox reaction). The log(*v*)-log(*i*) plots for the TiO₂@CNT@C nanorods are displayed in Figure 3b. The *b*-values of cathodic and anodic peaks are 0.81 and 0.83, respectively, which can be quantified at sweep rates ranging from 0.01 to 8 mV s⁻¹. It can be confirmed that the performance of sodium storage in TiO₂@CNT@C nanorods presents capacitive characteristics, conducing to improve the rate capability of active materials. The galvanostatic charge/discharge measurements in the range of 0.01–2.5 V are shown in Figure 3c–f. In Figure 3c, the TiO₂@CNT@C electrode delivers a moderate discharge capacity of 277 mA h g⁻¹ in the second cycle at the current density of 0.05 A g⁻¹, which is very close to the theoretical value of TiO₂. In the first cycle, the large capacity loss is attributed to the formation of solid electrolyte interface (SEI) films and decomposition of the electrolyte on the electrode surface during the Na⁺ insertion process. This problem could be solved through presodiation technique for practical applications to SIBs and hybrid devices. A previous report suggested that the sodium storage mechanism of TiO₂ was intercalation

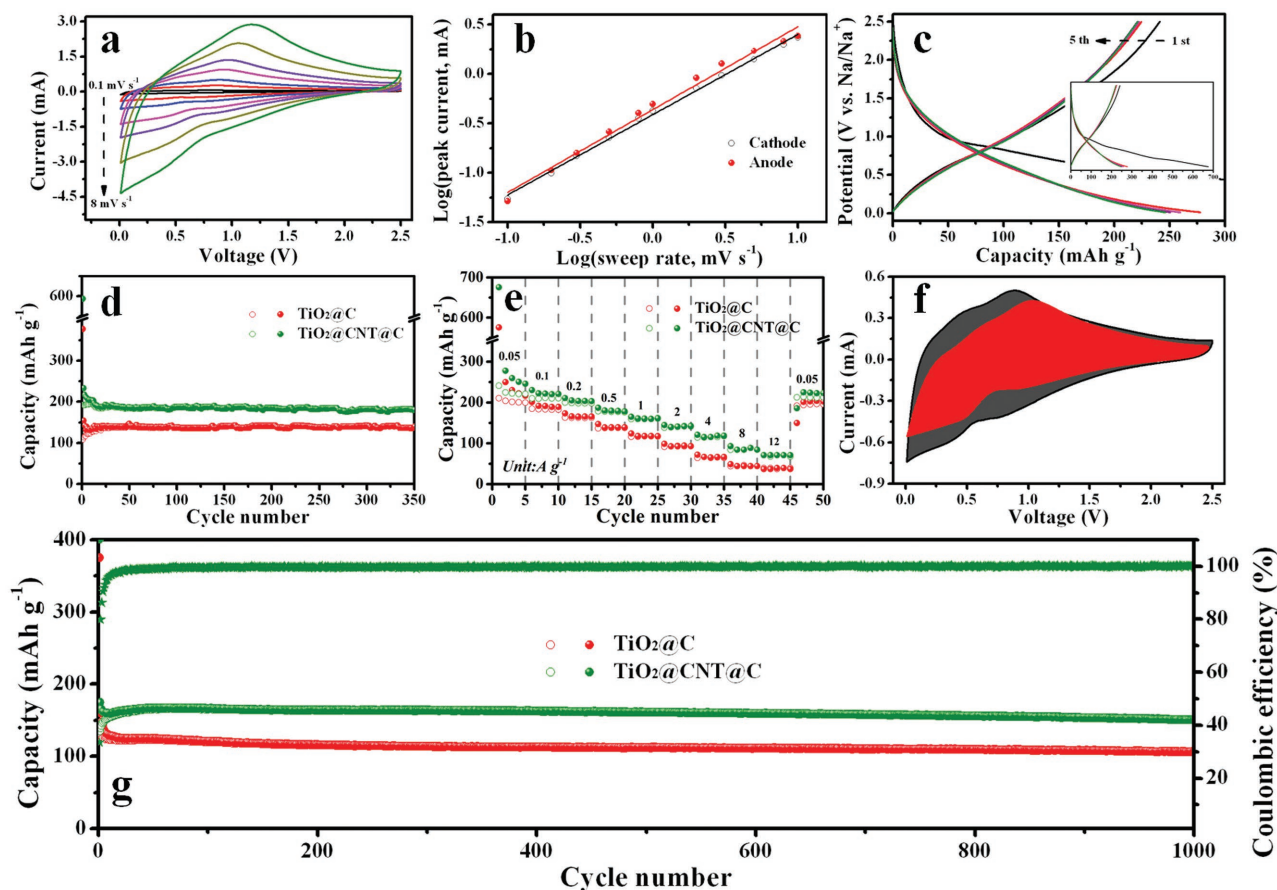


Figure 3. Electrochemical measurements of TiO₂@C and TiO₂@CNT@C/Na half cells. a,b) CV curves and specific peak current of TiO₂@CNT@C at various sweep rates from 0.1 to 8 mV s⁻¹. c) Typical galvanostatic charge/discharge profiles of TiO₂@CNT@C between 0.01 and 2.5 V at 0.05 A g⁻¹. d) The cycling capacity at 0.5 A g⁻¹. e) The rate performance and f) capacitive (red) and diffusion currents (gray) contributed to charge storage of TiO₂@CNT@C at a scan rate of 1 mV s⁻¹. g) The cycling capacity at 1 A g⁻¹, as well as the coulombic efficiency of TiO₂@CNT@C.

reaction^[41] as well as amorphization on the deep discharge in the first cycle, which are greatly coincident with the ex situ XRD of TiO₂@CNT@C (Figure S4, Supporting Information). The cycling performances of TiO₂@CNT@C and TiO₂@C electrodes are compared in Figure 3d. The reversible capacity of TiO₂@C electrodes only remained 139 mA h g⁻¹ after 350 cycles at 0.5 A g⁻¹. In the same case, the TiO₂@CNT@C electrode still achieved a high reversible capacity of 183 mA h g⁻¹ after 350 cycles, corresponding to 98% retention ratio of the capacity.

The rate performance of TiO₂@CNT@C and TiO₂@C is displayed in Figure 3e. The TiO₂@CNT@C electrode could deliver the reversible capacity of 230, 200, 159.6, 141.6, and 115.5 mA h g⁻¹ at 0.05, 0.2, 1, 2, and 4 A g⁻¹, respectively, which are demonstrated in the charge and discharge curves in Figure S3b (Supporting Information). Even at 8 and 12 A g⁻¹, the reversible capacity still reaches 85 and 71 mA h g⁻¹, respectively. When the current density goes back to 0.05 A g⁻¹, the reversible capacity could swiftly return to 213 mA h g⁻¹, exhibiting strong tolerance for fast sodiation/desodiation. Compared with the TiO₂@CNT@C electrode, the TiO₂@C anode exhibits relatively inferior rate performance. Moreover, the ratios of surface capacitive contribution and diffusion-controlled contribution are quantitatively separated through the method by Dunn and co-workers^[42,43]

$$i = k_1 \nu + k_2 \nu^{1/2} \quad (2)$$

In Equation (2), i is the current at a fixed potential, ν is the scan rate in the CV tests, and k_1 and k_2 are constants. $k_1\nu$ and $k_2\nu^{1/2}$ represent the surface capacitive and diffusion-controlled process, respectively. According to Equation (2), 70% of the total charge in the TiO₂@CNT@C electrode is surface capacitive (red region) at a sweep rate of 1 mV s⁻¹. Figure S5 (Supporting Information) shows that the ratios of capacitive contribution are improved gradually with increasing the sweep rate. The maximum values of TiO₂@CNT@C and TiO₂@C are 81 and 76% at 3 mV s⁻¹, respectively. The remarkable rate capability is attributed to the improved electrical conductivity and surface pseudocapacitance arising from the addition of MWCNTs as well as TiO₂ nanoparticles. Moreover, long-term cycling tests were also operated at the current density of 1 A g⁻¹, and the results are shown in Figure 3g. After the activation process in the initial 40 cycles, the capacity of the TiO₂@CNT@C electrode shows obvious increase from the initial 150 mA h g⁻¹ to the maximum value of 165 mA h g⁻¹. Unexpectedly, a high reversible capacity of 153 mA h g⁻¹ over 1000 cycles is achieved, corresponding to the capacity retention rate of 93% (based on the maximum capacity of 165 mA h g⁻¹). The cyclic stability of TiO₂@CNT@C is much better than that of most previously reported for Ti-based oxides.^[29,30,44,45] More interestingly, this is also distinguished performance among insertion-type materials (such as Nb₂O₅, Na₂Ti₆O₁₃, and hard carbon).^[46–48] The corresponding coulombic efficiency of the electrode was ≈100% (>99.7%) except the initial several cycles.

In order to further understand the effect of MWCNTs in TiO₂@CNT@C, electrochemical impedance spectroscopy (EIS) was performed, and the results are shown in Figure S6a (Supporting Information). The Nyquist plots consist of two typical

regions, a semicircle in the medium-to-high-frequency region and a slope curve in the low-frequency region. The diameter of the semicircle in the media-to-high-frequency region represents the charge-transfer resistance and the slope at low-frequency signifies Warburg impedance, which represents the solid-state diffusion of sodium in active materials.^[34] Obviously, TiO₂@CNT@C samples exhibit a lower charge transfer resistance than TiO₂@C due to the increased electrical conductivity in the presence of the MWCNTs. Figure S6b (Supporting Information) shows that the Warburg coefficient of TiO₂@CNT@C is smaller than that of TiO₂@C, demonstrating larger Na⁺ diffusion in TiO₂@CNT@C.^[49]

In addition, the performance of biomass-derived activated carbon (BAC) was measured in the potential range of 2.5–4.2 V versus Na/Na⁺. In Figure S7 (Supporting Information), the quasi-rectangular CV curves and linear charge–discharge profile confirm that the BAC cathode demonstrates electric double-layer capacitive behaviors with the surface adsorption/desorption process. The BAC cathode delivers an average discharge capacity of 50 mA h g⁻¹ at a current density of 0.5 A g⁻¹ and can also stably work for 2000 cycles with minor capacity loss, suggesting the highly robust adsorption/desorption process. The rate performances of BAC and commercial AC are compared in Figure S7f (Supporting Information). The AC cathode delivers inferior rate performances. The discharge capacity decreases quickly with increasing the current density, only retained 8 mA h g⁻¹ at 3 A g⁻¹. Surprisingly, the BAC cathode displays remarkable rate performances. The discharge capacity at various current densities from 0.2 to 3 A g⁻¹ shows no significant difference, even at the rate of 12 A g⁻¹; the BAC electrode could still deliver discharge capacity of ≈41 mA h g⁻¹, which indicates a quick charge propagation capability and facile ion transport arising from the large surface area (1438 m² g⁻¹) and abundant microchannels.

The full cells of Na-ion capacitors were assembled with TiO₂@CNT@C nanorods as the anode and BAC as the cathode. Considering the mismatch of the discharge capacity between the anode and cathode, we optimized the mass ratio of the active material for the anode and cathode. As shown in Figure S8 (Supporting Information), the results demonstrate that the optimal ratio of the two ends is determined to be 1:3 (the weight ratio of the anode and cathode, the same hereafter in this work) in the light of the highest energy/power density in the potential range of 1–4 V. The high potential window will facilitate the energy output of Na-ion capacitors. Figure 4a displays CV curves for Na-ion capacitors at the scan rate of 0.5–10 mV s⁻¹. The near-rectangular shapes of CV curves demonstrate the charge storage mechanisms of Na-ion capacitors, contributed from the combination of faradaic and nonfaradaic reactions. Figure 4b shows the typical charge/discharge profiles of Na-ion capacitors at different current densities, which present a near-linear correlation of ideal supercapacitor properties without diffusion-limited processes, which once again reveals interfacial electrochemical reactions with rapid energy storage kinetics. In the first charge of Na-ion capacitors, Na⁺ ions intercalate into the TiO₂@CNT@C electrode and interfacial regions from the electrolyte. In order to balance the charge in the electrolyte, ClO₄⁻ anions adsorb on the BAC electrode to form double layers. During the discharge process, a reversible route

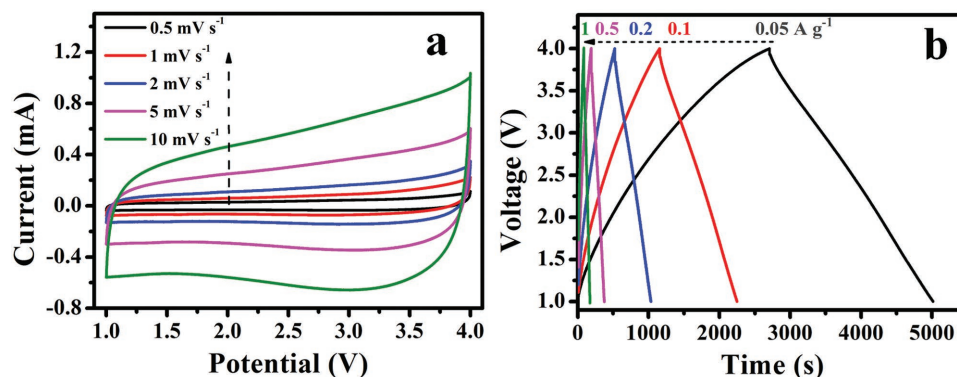


Figure 4. a) CV curves of the full cells at different scan rates, b) the typical charge/discharge plots of $\text{TiO}_2@\text{CNT}@\text{C}//\text{BAC}$ devices at various current densities in the range of 1.0–4.0 V.

is operated with ClO_4^- anions desorbing from the BAC electrode surface and Na^+ deintercalation from the $\text{TiO}_2@\text{CNT}@\text{C}$ electrode and interface. Furthermore, the inappreciable IR drop further demonstrates outstanding electrical conductivity. This phenomenon arises from the advanced architecture in both the anode and cathode and perfect kinetics match in the potential range of 1–4 V.

As expected, the Na-ion capacitors present a maximum energy density of 81.2 Wh kg^{-1} with the power density 126 W kg^{-1} achieved at 0.05 A g^{-1} (Figure 5a), which

is calculated from the active materials in both electrodes through Equations (3) and (4) (see Section 4).^[50] Even at ultrahigh power density of 12.4 kW kg^{-1} obtained at the current density of 6 A g^{-1} , the Na-ion capacitors still deliver an energy density of 37.9 Wh kg^{-1} (Figure 5a, and Figure S9, Supporting Information). Figure S10 (Supporting Information) shows the Ragone plots of $\text{TiO}_2@\text{CNT}@\text{C}//\text{BAC}$ full cells, compared with other devices. It is instructive to compare the electrochemical performances of $\text{TiO}_2@\text{CNT}@\text{C}//\text{BAC}$ full cells with many outstanding previously reported

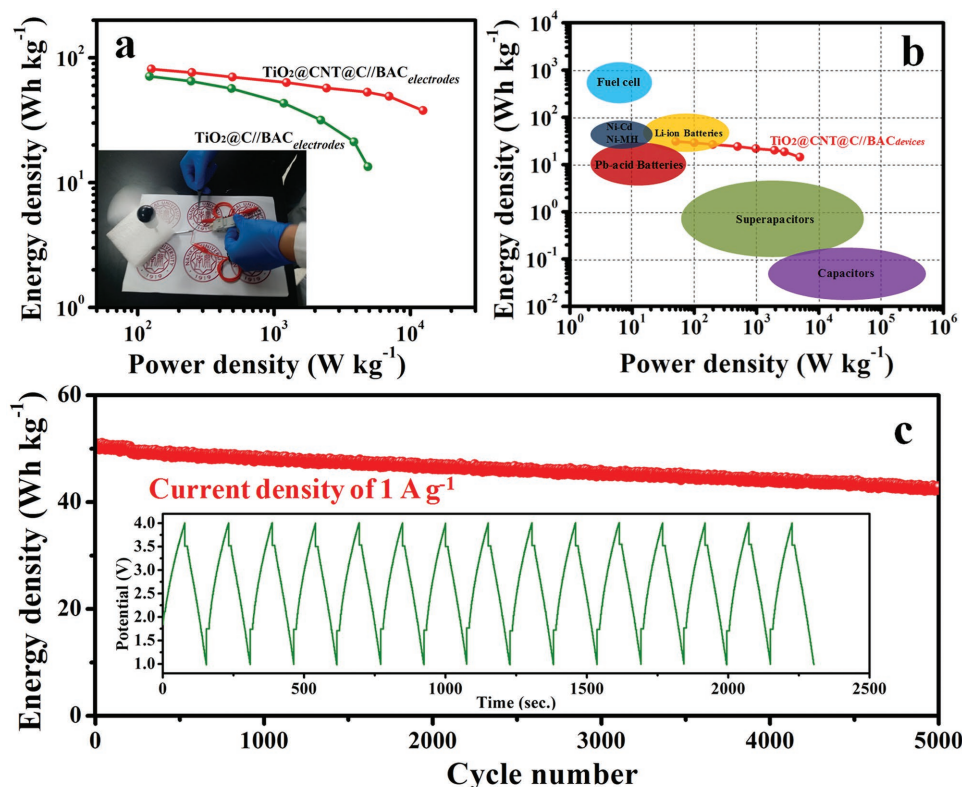


Figure 5. a) Ragone plots (energy density vs power density) of $\text{TiO}_2@\text{CNT}@\text{C}//\text{BAC}$ and $\text{TiO}_2@\text{C}//\text{BAC}$ full cells, b) device-based performance for the currently available energy-storage systems, c) long-term cycle performance at 1 A g^{-1} of $\text{TiO}_2@\text{CNT}@\text{C}//\text{BAC}$ full cells. The inset in panel (a) shows the fan driving application.

Li-ion capacitors and Na-ion capacitors to elucidate the suitable design. $\text{TiO}_2@\text{CNT}@\text{C}//\text{BAC}$ full cells outperform all the other Na-ion capacitors and comparable with similar Li-ion capacitors in the Ragone plots, demonstrating the exceptional energy/power delivery. Since the mass of active electrode materials makes up 35–40% of the total package,^[5,51,52] the Na-ion capacitors can obtain comparable energy density of commercial lithium-ion batteries, while the power density can also retain an appropriate value, which rivals the power density of supercapacitors (Figure 5b). For instance, the energy density based on the total package can reach up to 14.4 W h kg^{-1} at a package power density of 5 kW kg^{-1} , which indicates the synergistic effects of SIB-type anodes and capacitor-type cathodes in the hybrid system. The Na-ion capacitors act as a bridge between batteries and supercapacitors and fill the gaps in the field of current energy storage systems. Furthermore, the long-term cyclic tests were also performed for the Na-ion capacitors at 1 A g^{-1} (Figure 5c). The Na-ion capacitors display a degradation rate of capacitance of $0.0029\% \text{ cycle}^{-1}$ during 5000 cycles. The high coulombic efficiency ($\approx 100\%$) could further illustrate the excellent reversibility of the $\text{TiO}_2@\text{CNT}@\text{C}//\text{BAC}$ Na-ion capacitors (Figure S11, Supporting Information). Obviously, this state-of-the-art hybrid device well overcomes the intrinsic kinetics and capacity mismatch and provides suitable energy storage devices for large-scale applications. Finally, we evaluated the performance of the device in tentative applications by driving a mini fan. After fast charging, a single 4 V Na-ion capacitor could successfully drive a mini fan (inset of Figure 5a, Video S1, Supporting Information), which suggests high-voltage output and the potential of Na-ion capacitors for future practical applications.

3. Conclusion

In summary, we constructed a novel Na-ion capacitor with intercalation-type $\text{TiO}_2@\text{CNT}@\text{C}$ nanorods as the anode and high surface area biomass-derived active carbon as the cathode in an organic electrolyte. The $\text{TiO}_2@\text{CNT}@\text{C}$ anode, with excellent electrical conductivity and 1D nanoarchitecture, was prepared through a simple and flexible electrospinning method. Benefiting from the addition of MWCNTs and nano-sized TiO_2 particles, the $\text{TiO}_2@\text{CNT}@\text{C}$ electrode presented superior electrochemical performances, endowed with excellent rate capability, ultralong cyclic stability, and high capacity in half cells, demonstrating practical application as electrode materials for high-power Na-ion capacitors. Biomass-derived activated carbon, with high surface area and abundant pores, also delivered remarkable capacitance. Thanks to advantages of structures and properties in both the anode and cathode, the assembled $\text{TiO}_2@\text{CNT}@\text{C}//\text{BAC}$ hybrid capacitors displayed an exceptionally high energy density of 81.2 W h kg^{-1} and high power densities of $12\,400 \text{ W kg}^{-1}$, along with outstanding cyclic stability in the voltage window of $1.0\text{--}4.0 \text{ V}$. Those results show significant progress compared with available Li-ion capacitors and Na-ion capacitors and comparable energy density with commercial Li ion batteries. This work will offer a new approach to develop high-energy/power Na-ion capacitors as one of next-generation energy storage systems.

4. Experimental Section

Preparation of $\text{TiO}_2@\text{CNT}@\text{C}$ Nanorods and Control Groups: $\text{TiO}_2@\text{CNT}@\text{C}$ nanorods were prepared through a signal-nozzle electrospinning technique followed by a heat treatment. In the typical preparation, 0.8 g polyvinylpyrrolidone (PVP, average $M_w = 150\,000$) and 1.7 g tetrabutyl titanate ($\text{Ti}(\text{OC}_4\text{H}_9)_4$, 97%) were dissolved in 10 mL absolute ethanol with vigorous agitation for 24 h . Then 10 or 20 mg MWCNTs were added to the mixed solution with vigorous agitation for another 12 h . Subsequently, the precursor solution was loaded into a 10 mL plastic syringe equipped with a 21-gauge blunt tip needle. The flow rate of solution was set to $8 \mu\text{L min}^{-1}$ by a syringe pump. The needle was connected to a high-voltage power supply in order to apply a voltage of 15 kV between the needle and the collecting copper foil for the formation of nanorods. The distance between the needle and the copper foil was set to be 15 cm . Finally, the as-collected film was first stabilized at $80 \text{ }^\circ\text{C}$ for 6 h in an oven and stabilized at $260 \text{ }^\circ\text{C}$ for 1 h with a heating rate of $1 \text{ }^\circ\text{C min}^{-1}$, followed by carbonization at $500 \text{ }^\circ\text{C}$ for 2 h in Ar atmosphere with a heating rate of $2 \text{ }^\circ\text{C min}^{-1}$. For comparison, $\text{TiO}_2@\text{C}$ was obtained by the same method except the addition of MWCNTs.

Preparation of Active Carbon: To synthesize highly porous activated carbon, the fallen leaves of pear trees obtained from Jinnan Campus, Nankai University, were used as the raw materials. In the typical preparation, the fallen leaves were collected and cut into smaller pieces, washed with distilled water, and then dried at $65 \text{ }^\circ\text{C}$ for 24 h . The as-prepared leaves were carbonized at $500 \text{ }^\circ\text{C}$ for 2 h with a heating rate of $10 \text{ }^\circ\text{C min}^{-1}$ in Ar atmosphere and then ground. The precursor powder, K_2CO_3 and KOH with a weight ratio of $1:2:1$ were mixed and dissolved in distilled water with vigorous agitation for 2 h . After drying at $100 \text{ }^\circ\text{C}$, the mixture was pyrolyzed at $700 \text{ }^\circ\text{C}$ for 1 h under Ar atmosphere. The product was washed with 0.1 mol L^{-1} HCl solution and distilled water several times separately, to remove the residual K^+ . The final product was obtained after vacuum drying.

Materials Characterizations: The as-prepared samples were characterized by XRD (Rigaku D/Max III diffractometer with $\text{Cu K}\alpha$ radiation, $\lambda = 1.5418 \text{ \AA}$) and Raman spectroscopy (Renishaw inVia spectrometer, 514.5 nm Ar^+ laser). The morphologies were analyzed through a field-emission scanning electron microscope (FESEM, JEOL-JSM7500), HRTEM (FEI Tecnai, model G2F-20 field emission TEM), and selected area electron diffraction (SAED). N_2 adsorption–desorption isotherms were measured on a Quantachrome NOVA 2000e sorption analyzer at liquid nitrogen temperature (77 K). The specific surface area was obtained from BET analyses of the adsorption isotherms. The oxidation state and carbon contents of samples were detected by XPS (Axis Ultra DLD, Kratos Analytical) and thermogravimetry and differential thermal analysis (TG-DTA, Rigaku PTC-10A TG-DTA analyzer).

Fabrication of Half Cells: The working electrodes (both cathodes and anodes) consisted of $75 \text{ wt}\%$ active materials, $15 \text{ wt}\%$ acetylene black, and $10 \text{ wt}\%$ polyvinylidene fluoride (PVDF), which were dispersed in N-methyl-2-pyrrolidone (NMP) uniformly. The achieved slurry was pasted on current collectors (Cu foils for the $\text{TiO}_2@\text{CNT}@\text{C}$ anodes and Al foils for the biomass-derived activated carbon cathodes) and dried at $110 \text{ }^\circ\text{C}$ in a vacuum oven for 12 h . The working electrodes were punched out with diameters of 12 mm and mass loading of 1 mg cm^{-2} (anodes) and $2\text{--}4 \text{ mg cm}^{-2}$ (cathodes). In an Ar-filled glove box, CR2025-type coin cells were assembled. The electrolyte was a solution of 1 mol L^{-1} NaClO_4 in ethylene carbonate/propylene carbonate (EC/PC, 1:1 in volume). Metallic sodium was selected as the counter electrode and glass fibers were used as the separator. The coin cells were cycled in a potential range of $0.01\text{--}2.5 \text{ V}$ for anodes and $2.5\text{--}4.2 \text{ V}$ for cathodes on a LAND CT2001 tester at different rates. CV tests were performed on a CHI600A electrochemical workstation (Shanghai Chenhua). EIS was performed on a Zahner-Elektrik IM6e electrochemical workstation by sweeping the frequency from 100 kHz to 10 mHz with an AC amplitude of 5 mV .

Fabrication of Hybrid Devices: Before assembling the full cell, $\text{TiO}_2@\text{CNT}@\text{C}$ was precycled five times at 0.05 A g^{-1} in half cells. Na-ion capacitors were assembled in coin cells with presodiated $\text{TiO}_2@\text{CNT}@\text{C}$ as the anode, BAC as the cathode, and the glass fibers as the separator.

The applied electrolyte was the same as that in half cells. In order to achieve optimized energy and power density of Na-ion capacitors, the mass ratio between the TiO₂@CNT@C anode and BAC cathode was selected 1:2, 1:3, and 1:4 in the voltage range of 1.0–4.0 V. Note that the current densities were based on the total mass of active materials in both the anode and cathode. The energy and power density of full cells were calculated by numerically integrating the galvanostatic discharge curves by using the equations below

$$E = \int_{t_1}^{t_2} IV dt \quad (3)$$

$$P = \frac{E}{t} \quad (4)$$

In the above equations, I is the constant current density (A g⁻¹), V (V) is the working voltage, t_1 and t_2 are the start and end of discharge time (s) of Na-ion capacitors, respectively, and t is the discharge time (s).

Supporting Information

Supporting Information is available from the Wiley Online Library or from the author.

Acknowledgements

This work was supported by MOST (2016YFA0200200) in China.

Conflict of Interest

The authors declare no conflict of interest.

Keywords

high power, long cycle life, Na-ion capacitors, sodium ion batteries, TiO₂

Received: May 4, 2017

Revised: June 11, 2017

Published online: August 25, 2017

- [1] B. Dunn, H. Kamath, J.-M. Tarascon, *Science* **2011**, 334, 928.
 [2] J. B. Goodenough, Y. Kim, *Chem. Mater.* **2010**, 22, 587.
 [3] D. Pech, M. Brunet, H. Durou, P. Huang, V. Mochalin, Y. Gogotsi, P. L. Taberna, P. Simon, *Nat. Nanotechnol.* **2010**, 5, 651.
 [4] Y. Zhu, S. Murali, M. D. Stoller, K. J. Ganesh, W. Cai, P. J. Ferreira, A. Pirkle, R. M. Wallace, K. A. Cychoz, M. Thommes, D. Su, E. A. Stach, R. S. Ruoff, *Science* **2011**, 332, 1537.
 [5] M. Yang, Y. Zhong, J. Ren, X. Zhou, J. Wei, Z. Zhou, *Adv. Energy Mater.* **2015**, 5, 1500550.
 [6] P. Simon, Y. Gogotsi, *Nat. Mater.* **2008**, 7, 845.
 [7] V. Aravindan, J. Gnanaraj, Y. S. Lee, S. Madhavi, *Chem. Rev.* **2014**, 114, 11619.
 [8] H. Pan, Y.-S. Hu, L. Chen, *Energy Environ. Sci.* **2013**, 6, 2338.
 [9] N. Yabuuchi, M. Kajiyama, J. Iwatate, H. Nishikawa, S. Hitomi, R. Okuyama, R. Usui, Y. Yamada, S. Komaba, *Nat. Mater.* **2012**, 11, 512.
 [10] N. Yabuuchi, K. Kubota, M. Dahbi, S. Komaba, *Chem. Rev.* **2014**, 114, 11636.
 [11] Y.-E. Zhu, L. Yang, X. Zhou, F. Li, J. Wei, Z. Zhou, *J. Mater. Chem. A* **2017**, 5, 9528.
 [12] D. Chao, C. Zhu, P. Yang, X. Xia, J. Liu, J. Wang, X. Fan, S. V. Savilov, J. Lin, H. J. Fan, Z. X. Shen, *Nat. Commun.* **2016**, 7, 12122.
 [13] E. Lim, C. Jo, M. S. Kim, M. H. Kim, J. Chun, H. Kim, J. Park, K. C. Roh, K. Kang, S. Yoon, J. Lee, *Adv. Funct. Mater.* **2016**, 26, 3711.
 [14] H. Li, Y. Zhu, S. Dong, L. Shen, Z. Chen, X. Zhang, G. Yu, *Chem. Mater.* **2016**, 28, 5753.
 [15] S. Dong, L. Shen, H. Li, G. Pang, H. Dou, X. Zhang, *Adv. Funct. Mater.* **2016**, 26, 3703.
 [16] J. Ding, H. L. Wang, Z. Li, K. Cui, D. Karpuzov, X. H. Tan, A. Kohandehghan, D. Mitlin, *Energy Environ. Sci.* **2015**, 8, 941.
 [17] Z. Le, F. Liu, P. Nie, X. Li, X. Liu, Z. Bian, G. Chen, H. B. Wu, Y. Lu, *ACS Nano* **2017**, 11, 2952.
 [18] V. Aravindan, M. Ulaganathan, S. Madhavi, *J. Mater. Chem. A* **2016**, 4, 7538.
 [19] J. Yin, L. Qi, H. Wang, *ACS Appl. Mater. Interfaces* **2012**, 4, 2762.
 [20] R. Thangavel, K. Kaliyappan, K. Kang, X. Sun, Y.-S. Lee, *Adv. Energy Mater.* **2016**, 6, 1502199.
 [21] Y. Ma, H. Chang, M. Zhang, Y. Chen, *Adv. Mater.* **2015**, 27, 5296.
 [22] Y. Wang, Y. Song, Y. Xia, *Chem. Soc. Rev.* **2016**, 45, 5925.
 [23] Y. S. Hu, L. Kienle, Y. G. Guo, J. Maier, *Adv. Mater.* **2006**, 18, 1421.
 [24] J. Chen, W. Song, H. Hou, Y. Zhang, M. Jing, X. Jia, X. Ji, *Adv. Funct. Mater.* **2015**, 25, 6793.
 [25] Y. Wu, X. Liu, Z. Yang, L. Gu, Y. Yu, *Small* **2016**, 12, 3522.
 [26] L. Wu, D. Bresser, D. Buchholz, G. A. Giffin, C. R. Castro, A. Ochel, S. Passerini, *Adv. Energy Mater.* **2015**, 5, 1401142.
 [27] W. Jiao, N. Li, L. Wang, L. Wen, F. Li, G. Liu, H. M. Cheng, *Chem. Commun.* **2013**, 49, 3461.
 [28] X. Lu, W. Yang, Z. Quan, T. Lin, L. Bai, L. Wang, F. Huang, Y. Zhao, *J. Am. Chem. Soc.* **2014**, 136, 419.
 [29] C. Chen, Y. Wen, X. Hu, X. Ji, M. Yan, L. Mai, P. Hu, B. Shan, Y. Huang, *Nat. Commun.* **2015**, 6, 6929.
 [30] Y. Zhang, C. W. Foster, C. E. Banks, L. Shao, H. Hou, G. Zou, J. Chen, Z. Huang, X. Ji, *Adv. Mater.* **2016**, 28, 9391.
 [31] H. Han, T. Song, J.-Y. Bae, L. F. Nazar, H. Kim, U. Paik, *Energy Environ. Sci.* **2011**, 4, 4532.
 [32] K. Tang, Y. Yu, X. Mu, P. A. van Aken, J. Maier, *Electrochem. Commun.* **2013**, 28, 54.
 [33] R. Mo, Z. Lei, K. Sun, D. Rooney, *Adv. Mater.* **2014**, 26, 2084.
 [34] Y. Zhong, M. Yang, X. Zhou, Y. Luo, J. Wei, Z. Zhou, *Adv. Mater.* **2015**, 27, 806.
 [35] M. Yang, Y. R. Zhong, J. Bao, X. L. Zhou, J. P. Wei, Z. Zhou, *J. Mater. Chem. A* **2015**, 3, 11387.
 [36] H. Kim, M.-Y. Cho, M.-H. Kim, K.-Y. Park, H. Gwon, Y. Lee, K. C. Roh, K. Kang, *Adv. Energy Mater.* **2013**, 3, 1500.
 [37] H. B. Wu, G. Zhang, L. Yu, X. W. Lou, *Nanoscale Horiz.* **2016**, 1, 27.
 [38] H. Gu, Y.-E. Zhu, J. Yang, J. Wei, Z. Zhou, *ChemNanoMat* **2016**, 2, 578.
 [39] K. J. Jeon, H. R. Moon, A. M. Ruminiski, B. Jiang, C. Kisielowski, R. Bardhan, J. J. Urban, *Nat. Mater.* **2011**, 10, 286.
 [40] H. Lindström, S. Södergren, A. Solbrand, H. Rensmo, J. Hjelm, A. Hagfeldt, S.-E. Lindquist, *J. Phys. Chem. B* **1997**, 101, 7717.
 [41] Y. Xiong, J. F. Qian, Y. L. Cao, X. P. Ai, H. X. Yang, *J. Mater. Chem. A* **2016**, 4, 11351.
 [42] V. Augustyn, J. Come, M. A. Lowe, J. W. Kim, P. L. Taberna, S. H. Tolbert, H. D. Abruna, P. Simon, B. Dunn, *Nat. Mater.* **2013**, 12, 518.
 [43] J. Wang, J. Polleux, J. Lim, B. Dunn, *J. Phys. Chem. C* **2007**, 111, 14925.

- [44] Y. Xiong, J. Qian, Y. Cao, X. Ai, H. Yang, *ACS Appl. Mater. Interfaces* **2016**, *8*, 16684.
- [45] J. P. Huang, D. D. Yuan, H. Z. Zhang, Y. L. Cao, G. R. Li, H. X. Yang, X. P. Gao, *RSC Adv.* **2013**, *3*, 12593.
- [46] L. Wang, X. Bi, S. Yang, *Adv. Mater.* **2016**, *28*, 7672.
- [47] K. Cao, L. Jiao, W. K. Pang, H. Liu, T. Zhou, Z. Guo, Y. Wang, H. Yuan, *Small* **2016**, *12*, 2991.
- [48] Y. Li, Y.-S. Hu, M.-M. Titirici, L. Chen, X. Huang, *Adv. Energy Mater.* **2016**, *6*, 1600659.
- [49] Y. Zhu, T. Gao, X. Fan, F. Han, C. Wang, *Acc. Chem. Res.* **2017**, *50*, 1022.
- [50] R. Yi, S. R. Chen, J. X. Song, M. L. Gordin, A. Manivannan, D. H. Wang, *Adv. Funct. Mater.* **2014**, *24*, 7433.
- [51] F. Zhang, T. Zhang, X. Yang, L. Zhang, K. Leng, Y. Huang, Y. Chen, *Energy Environ. Sci.* **2013**, *6*, 1623.
- [52] J. J. Ren, L. W. Su, X. Qin, M. Yang, J. P. Wei, Z. Zhou, P. W. Shen, *J. Power Sources* **2014**, *264*, 108.